WILEY | Hindawi

Research Article

High-Entropy Carbonates (Ni-Mn-Co-Zn-Cr-Fe) as a Promising Electrocatalyst for Alkalized Seawater Oxidation

Min Gi Kim,[1] **Ashish Gaur,**[1] **Jin Uk Jang,**[2] **Kyeong-Han Na,**[3,4] **Won-Youl Choi** [3,4] **and HyukSu Han** [1]

[1]*Department of Energy Science, Sungkyunkwan University, Suwon 16419, Republic of Korea*
[2]*Department of Energy Engineering, Konkuk University, 120 Neungdong-ro, Seoul 05029, Republic of Korea*
[3]*Department of Metal and Materials Engineering, Gangneung-Wonju National University, 7 Jukheongil, Gangneung, Gangwon 25457, Republic of Korea*
[4]*Smart Hydrogen Energy Center, Gangneung-Wonju National University, 7 Jukheongil, Gangneung, Gangwon 25457, Republic of Korea*

Correspondence should be addressed to Won-Youl Choi; cwy@gwnu.ac.kr and HyukSu Han; hyuksuhan@skku.edu

Direct seawater splitting has attracted considerable attention as an alternative to conventional alkaline water electrolysis because the former avoids the use of limited freshwater resources. However, several challenges must be overcome to realize direct seawater electrolysis. Most importantly, electrocatalysts for the anodic oxygen evolution reaction (OER) should exhibit high activity, stability, and selectivity in highly corrosive environments with abundant chloride ions. In this study, we developed high-entropy carbonate (HEC) as a promising electrocatalyst for seawater oxidation. In HECs, physicochemical interactions among different elements can effectively suppress the corrosion of OER active sites, while polyanionic CO_3^{2-} can act as a corrosion-protective species by repelling negatively charged chloride ions during electrolysis. Consequently, HECs demonstrate outstanding catalytic activity, stability, and selectivity for seawater oxidation, surpassing those of ternary, quaternary, and quinary carbonates and even benchmark IrO_2 catalysts.

1. Introduction

Hydrogen is considered the ultimate clean fuel owing to its sustainability and high energy density of $142\,MJ\,kg^{-1}$ [1]. In this context, water electrolysis offers a promising route for producing green (clean) hydrogen without emitting carbonaceous byproducts such as CO_2 [2]. Water electrolysis occurs through two half-reactions: the two-electron transfer hydrogen evolution reaction (HER) at the cathode and the four-electron transfer oxygen evolution reaction (OER) at the anode. Compared to the HER, the OER shows slow reaction kinetics with a complicated proton-electron transfer process, which limits the overall water-splitting efficiency [3]. To facilitate the OER kinetics for efficient water splitting, researchers have devoted enormous efforts to designing novel catalysts with low overpotential and high stability

[4]. To date, IrO_2/RuO_2 catalysts have been recognized as benchmark catalysts for the OER, but the high cost and scarcity of precious metals hinder their industrial commercialization [5].

In addition, most of the current studies on water electrolysis focus on freshwater as a feedstock for producing hydrogen. However, considering the high worldwide demand for fresh water, earth-abundant seawater could be a quasi-infinitive resource for water splitting. Thus, the development of highly efficient noble metal-free electrocatalysts for seawater splitting is anticipated and remains challenging [6]. In this context, very recently several noble metal-free systems such as layered double hydroxides (LDHs) [7], alloys [8], oxides [9], selenides [10], borides [11], and nitrides [12] have been employed for seawater electrolysis. However, the presence of chloride (Cl^-) ions in seawater severely affects or damages

electrode materials during electrolysis through thermodynamically favorable chloride corrosion [13]. Furthermore, during seawater oxidations, chloride evolution reaction (CER) is competing with OER at the anode with an overpotential difference of 480 mV (pH 13) [14]. This can significantly lower the faradaic efficiency of hydrogen production when seawater is used as feedstock. Therefore, the development of an efficient and stable anode catalyst with high selectivity is indispensable for promoting the OER in seawater.

Recently, high-entropy materials (HEMs) have gained considerable attention as promising electrocatalysts owing to their excellent corrosion resistance resulting from synergetic physicochemical interactions among various constituent elements in a single-phase crystal structure [15]. In HEMs, high-entropy stabilization effects, ΔS_{mix} higher than 1.5, lead to a uniform distributions of elements in a low Gibbs free energy states, and thus, the galvanic corrosion can be effectively suppressed [16]. In addition, the difference in atomic size of mixed elements in HEMs can readily induce lattice distortion increasing energy barrier for atomic diffusions, which could be also beneficial for preventing dissolutions of catalytic elements into the electrolyte during electrolysis [17]. Furthermore, the synergistic effects of multiple components in HEMs can improve ligand and strain effects tailoring the electronic configurations of catalysts by shifting the d-band centers, which is advantageous for enhancing catalytic activity [18]. Various types of HEMs, such as high-entropy oxides and high-entropy alloys, have recently been recognized as promising HER and OER electrocatalysts compared to perovskite and spinel oxides, owing to their higher redox behavior, better corrosion resistance and oxygen evolution kinetics, and greater chemical durability and flexibility [19]. Thus, it is important to develop new HEMs for OER in seawater.

Herein, we demonstrate for the first time that high-entropy carbonates (HECs) composed of nickel-manganese-cobalt-zinc-chromium-iron carbonate (NMCZCrFe) are promising materials for seawater oxidation. NMCZCrFe was synthesized using a facile hydrothermal method. The optimized NMCZCrFe showed excellent OER performance in alkalized seawater, superior to that of its counterparts, including ternary carbonates, quaternary carbonates, and a benchmark IrO_2 catalyst. In addition, the as-synthesized NMCZCrFe exhibited excellent durability for seawater oxidation with high selectivity for the OER. The improved catalytic activity, stability, and selectivity of NMCZCrFe for seawater oxidation were attributed to its highly entropic platform nature and polyanionic carbonate species.

2. Materials and Methods

2.1. Chemicals.
For the synthesis of HECs, nickel(II) nitrate hexahydrate ($Ni(NO_3)_2 \cdot 6H_2O$, 99.9%), manganese(II) nitrate hexahydrate ($Mn(NO_3)_2 \cdot 6H_2O$, 98%), cobalt(II) nitrate hexahydrate ($Co(NO_3)_2 \cdot 6H_2O$, 99%), zinc nitrate hexahydrate ($Zn(NO_3)_2 \cdot 6H_2O$, 98%), chromium(III) nitrate nonahydrate ($Cr(NO_3)_2 \cdot 9H_2O$, 99.9%), iron(III) nitrate nonahydrate ($Fe(NO_3)_2 \cdot 9H_2O$, 98%), urea, polyvinylpyrrolidone (PVP, average mol wt 40,000), isopropyl alcohol (IPA), and Nafion

solution (5% wt/wt) were purchased from Sigma-Aldrich (Germany). Carbon black was purchased from TCK Inc., and (1-hexadecyl)trimethylammonium bromide (CTAB, 98%) was purchased from Alfa Aesar. All chemicals were purchased without further treatment.

2.2. Material Synthesis

2.2.1. Synthesis of Ternary (Ni-Mn-Co (NMC)) Carbonate.
All precursors $Ni(NO_3)_2 \cdot 6H_2O$, $Mn(NO_3)_2 \cdot 6H_2O$, and $Co(NO_3)_2 \cdot 6H_2O$, each weighing 0.25 g, were placed in a 100 mL beaker containing 50 mL deionized (DI) water. Then, 0.75 g of PVP, 6 g of urea, and 1 g of CTAB were mixed and stirred for 30 min. After that, the resulting solution was transferred to a Teflon-lined stainless steel autoclave (100 mL) and subjected to hydrothermal synthesis at 150°C for 4 h. After cooling, the solution was centrifuged and a brown precipitate was obtained. The obtained precipitate product was further dried in an oven at 80°C for 12 h to collect the nickel-manganese-cobalt carbonate powder and named as NMC.

2.2.2. Synthesis of HECs.
All HECs were synthesized using the same procedure as that for NMC, and an appropriate amount of precursor was added per composition. During the synthesis of NMC powder, we added 0.25 g of $Zn(NO_3)_2 \cdot 6H_2O$ for NMCZ, 0.25 g of $Cr(NO_3)_2 \cdot 9H_2O$ for NMCCr, 0.1 g of $Fe(NO_3)_2 \cdot 9H_2O$ for NMCF, 0.25 g each Zn and Cr precursors for NMCZCr, and 0.25 g Zn and Cr precursors and 0.1 g Fe precursor for NMCZCrFe, keeping the rest of the synthesis parameters fixed.

2.3. Characterizations

2.3.1. Fourier Transform Infrared (FTIR) Spectroscopy.
To investigate the nature of the chemical bonds in the samples, Fourier transform infrared (FTIR) spectroscopy (FT/IR-4100, Jasco) was performed.

2.3.2. Thermogravimetric Analysis (TGA).
Thermogravimetric analysis (TGA; SDT Q600, TA Instruments) was used to measure the mass changes of the samples at different temperatures. The temperature was raised 10°C/min under nitrogen and heated from room temperature to 800°C.

2.3.3. Scanning Electron Microscopy (SEM).
Scanning electron microscopy (SEM model S4800, Hitachi) was used to examine the morphology of the samples.

2.3.4. Transmission Electron Microscopy (TEM).
TEM (Talos F200X, Thermo Fisher Scientific) was used to collect the microstructures, and an energy dispersive X-ray (EDX) spectroscopy setup, including the TEM, was employed to determine the elemental distributions of the samples.

2.3.5. Powder X-Ray Diffraction (XRD).
X-ray diffraction (XRD) data were collected using Cu Kα radiation at 40 kV and 100 mA. An X-ray diffractometer (Rigaku D/Max 2550) was used.

2.3.6. X-Ray Photoelectron Spectroscopy (XPS).
X-ray photo-electron spectroscopy (XPS; VG ESCALAB 200i, Thermo Fisher Scientific) was used to determine the surface electronic structure of the samples. Energy calibration of the spectrometer was performed using the C-peak position. Pass energies of 100 and 20 eV were used for the survey and high-resolution scans, respectively.

2.3.7. Inductively Coupled Plasma-Optical Emission Spectroscopy (ICP-OES).
To calculate the composition of each NMCZCrFe sample, inductively coupled plasma-optical emission spectroscopy (ICP-OES; Thermo Scientific, iCAP6500 Duo) was used. The power and wavelength were set to 1350 W and 214.42 nm, respectively.

2.4. Electrochemical Measurements

2.4.1. Three-Electrode Measurement.
The electrocatalytic performance was evaluated using a three-electrode system connected to a potentiostat (Autolab PGSTAT, Metrohm) under simulated seawater conditions (1 M KOH and 0.5 M NaCl). The catalyst ink was prepared through a dispersion of 5 mg carbon black and 5 mg catalyst in 900 μL DI water, 50 μL IPA, and 50 μL Nafion 117 solution. After 30 min of sonication, the prepared catalyst ink was loaded onto the substrate (carbon cloth (CC), area = 0.25 cm^2) with a quantity of 13.8 μL, and it was used as the working electrode. The preparation process of the substrate is as follows: CC was cleaned in a mixture of nitric acid and DI water at a volume ratio of 3 : 1 for 1 h at 100°C. The resulting solution was stirred at 100 rpm for 1 h and washed several times with water and ethanol. The cleaned CC were then dried for 12 h at room temperature.

An Ag/AgCl electrode served as the reference electrode, while a Pt sheet was used as the counter electrode. Before electrochemical measurements, the electrolyte was purged with Ar gas for approximately 25 min. Subsequently, the catalyst' surface was electrochemically stabilized through 50 cycles of cyclic voltammetry (CV) in the OER potential range. Subsequently, linear sweep voltammetry (LSV) curves were recorded at a scan rate of 5 mV/s. The measured potentials were calibrated against the reversible hydrogen electrode (RHE) voltage. Additionally, iR correction was applied to all LSV curves unless otherwise stated. Electrochemical impedance spectroscopy (EIS) was conducted at 0.6 V$_{RHE}$ over a frequency range of 0.1–100 kHz with a sinusoidal amplitude of 5 mV. The Tafel plots were obtained using the iR-corrected LSV polarization curves. The Tafel slopes were determined using the following equation: $\eta = b \log j + a$, where b is the Tafel slope (mV/dec), j is the current density (mA cm^{-2}), and η is the overpotential (mV).

2.4.2. Determination of Electrochemical Double-Layer Capacitance (C_dl).
CVs were measured in the non-Faradic potential range (e.g., 1.1–1.2 V$_{RHE}$) at different scan rates (20–120 mV/s) in 1 M KOH solution (saturated with O$_2$) to estimate the double-layer capacitance (C_{dl}). The difference between the anodic and cathodic currents ($\Delta J = J_{anodic} - J_{cathodic}$) in the middle of the potential (1.15 V$_{RHE}$) was plotted against the scan rate, in which the slope corresponded to twice the C_{dl} of the catalyst. The equation used for C_{dl} is as follows:

$$C_{dl} = \frac{j_{a-j_c}}{2 \times v} = \frac{j_a + |j_c|}{2 \times v} = \frac{\Delta j}{2 \times v}. \tag{1}$$

Here, j_a and j_c represent the anodic and cathodic current densities, respectively, recorded at the midpoint of the selected potential range, and v is the sweep rate.

2.4.3. Determination of Electrochemical Surface Area (ECSA).
The electrochemically active surface area (ECSA) of the sample was determined from the measured C_d, in which a flat surface area of 1 cm^2 is approximately corresponding to the specific capacitance of 40 μF cm^{-2}. The ECSA of the catalyst was estimated using the following equation:

$$ECSA = \frac{C_{dl} \text{ of catalyst } \left(\mu F\, cm^{-2}\right)}{0.04 \left(\mu F\, cm^{-2}\right)}. \tag{2}$$

2.4.4. Determination of Turnover Frequency (TOF).
The turnover frequency (TOF) was calculated using the following equation:

$$TOF = j \times \frac{A}{4 \times F \times N_s}, \tag{3}$$

where j is the current density at a specific potential (Acm^{-2}), A is the surface area of the working electrode (cm^{-2}), F is the Faraday constant (96,458 Cmol^{-1}), and N_s is the concentration of active sites (mol cm^{-2}). The value of N_s was determined by CV measurements, in which the oxidative peak currents generated by the active sites exhibited a linear relationship at different scan rates. The slope in the linear plot is equal to

$$slope = \frac{n^2 F^2 A N_s}{4RT}, \tag{4}$$

where n, F, A, N_s, R, and T represent the number of electrons transferred, Faraday constant, electrode surface area, active site surface concentration, ideal gas constant, and temperature, respectively.

2.4.5. Determination of Faradaic Efficiency Using Rotating Ring Disk Electrode (RRDE).
To calculate the Faradaic efficiency (FE) for the OER, a Pt ring disc was applied by a potential of 0.6 V$_{RHE}$ to reduce O$_2$ which were generated from the disc electrode via OER by supplying a constant current of 1.96 mA. The FE can be calculated as

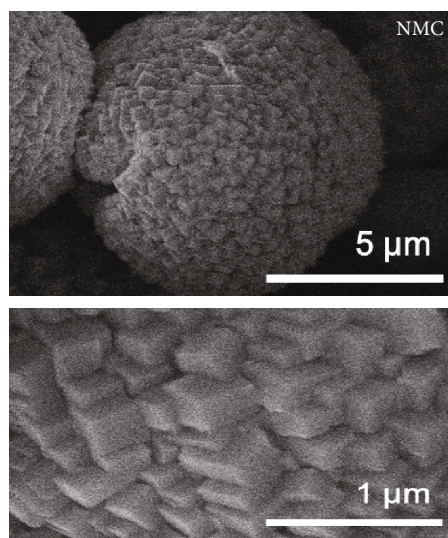$$FE = \frac{i_d - \lceil i_r \rceil / N}{i_d}, \tag{5}$$

where i_d, i_r, and N are the disk current, ring current, and current collection efficiency, respectively, and FE was determined to be approximately 0.23 for our RRDE system.
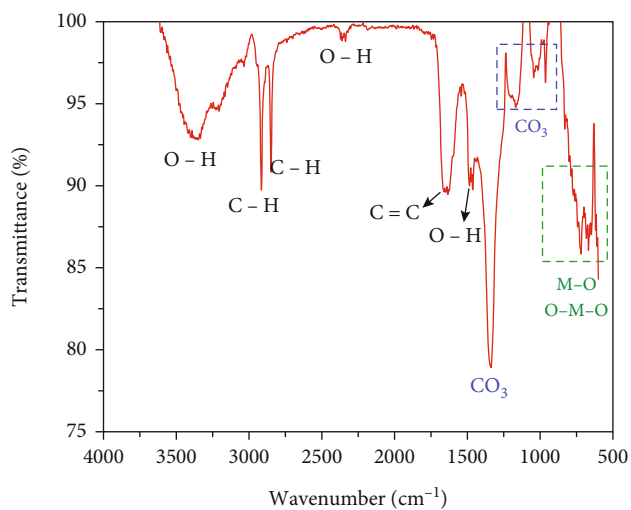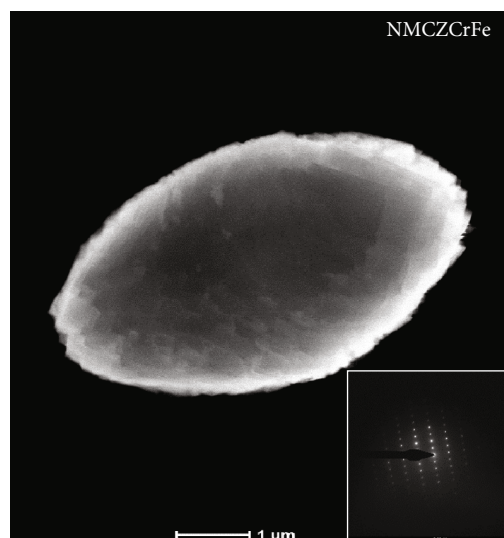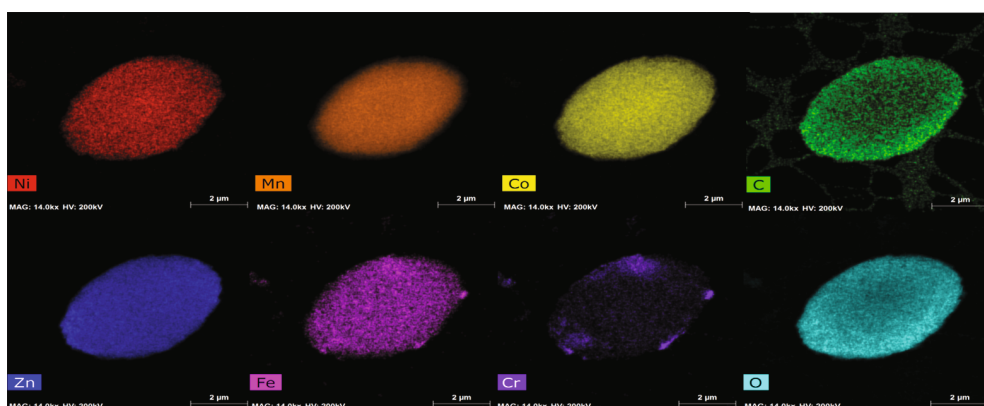
(a)
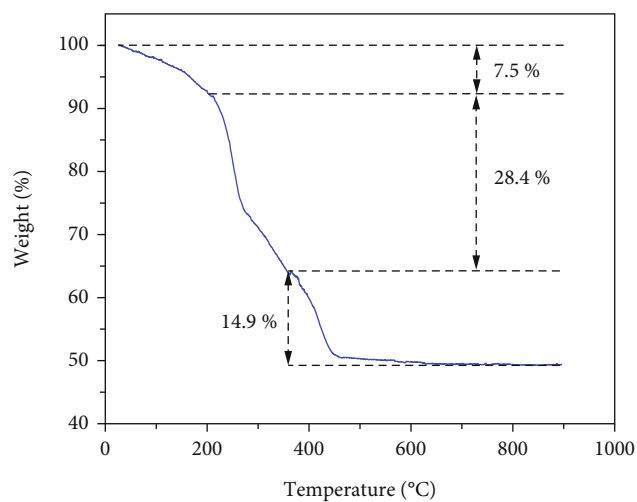
(b)
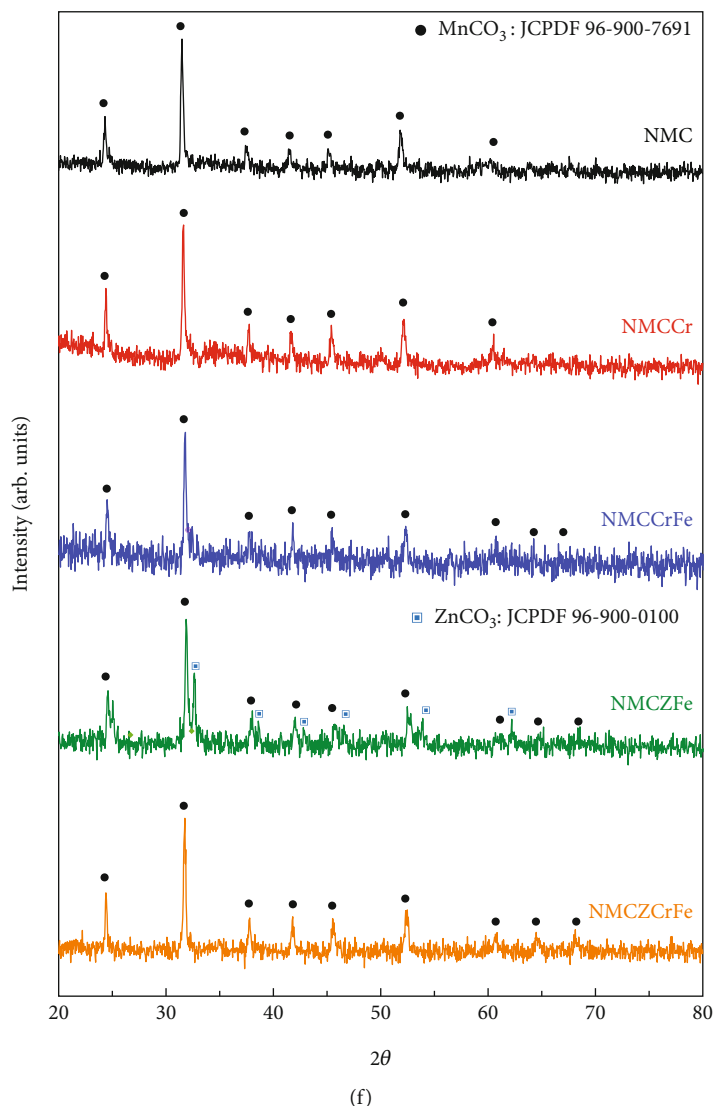

(c)

(d)

(e)

Figure 1: Continued.

(f)

FIGURE 1: (a) FTIR spectra and (b) TGA profile of NMCZCrFe. (c) SEM images of NMC. (d) STEM image of NMCZCrFe (HECs) and (e) STEM-EDX mapping results. (f) XRD patterns of the different carbonate samples.

3. Results and Discussion

The high-entropy carbonates (HECs) containing Ni, Mn, Co, Zn, Cr, and Fe (NMCZCrFe) were synthesized using solution phase method. The chemical bonding structures of the synthesized HEC (NMCZCrFe) powder were identified by FTIR spectroscopy (Figure 1(a)). Hereafter, HECs indicate the NMCZCrFe samples if not specifically mentioned. The obtained spectra matched the typical patterns of carbonates [18]. Specifically, the broad band at 3380 cm^{-1} is associated with the O–H stretching vibrations of surface hydroxyl groups or adsorbed water molecules [18]. Narrow bands at 1340, 1170, and 960 are attributed to the vibrations of carbonates in stretching or bending modes [20]. In addition, lattice vibrations of metal and oxygen (e.g., M–O or O–M–O) were observed at low wave numbers (550–800 cm^{-1}), supporting a successful formation of metal carbonate phase in the prepared HEC powder. Figure 1(b) shows the TGA curve of MEC powder. A weight loss below 200°C is ascribed

to thermal evaporation or decomposition of adsorbed water on the surface. Subsequently, an abrupt weight loss occurred at temperatures above 300°C, which can be attributed to the phase transformation of carbonates to oxides involving thermal decomposition of carbonates [21].

The microstructures of the synthesized powders were studied using SEM. A pristine ternary carbonate (NMC) powder was formed in microspheres with a diameter of approximately 3–5 μm (Figure 1(c) and Figure S1). During hydrothermal reactions, polymers derived from PVP or IPA may act as capping agents that are radially adsorbed on the surface of the nuclei, facilitating the spherical growth of nucleated particles. Furthermore, the surface of the NMC carbonate exhibited a hierarchical morphology consisting of nanocubes, which possibly enhanced the number of catalytic active sites. After adding three more elements (Zn, Fe, and Cr) to the NMC, the HECs exhibited an elliptical morphology with a highly crystalline nature (Figure 1(d)). Notably, the STEM-EDX mapping results
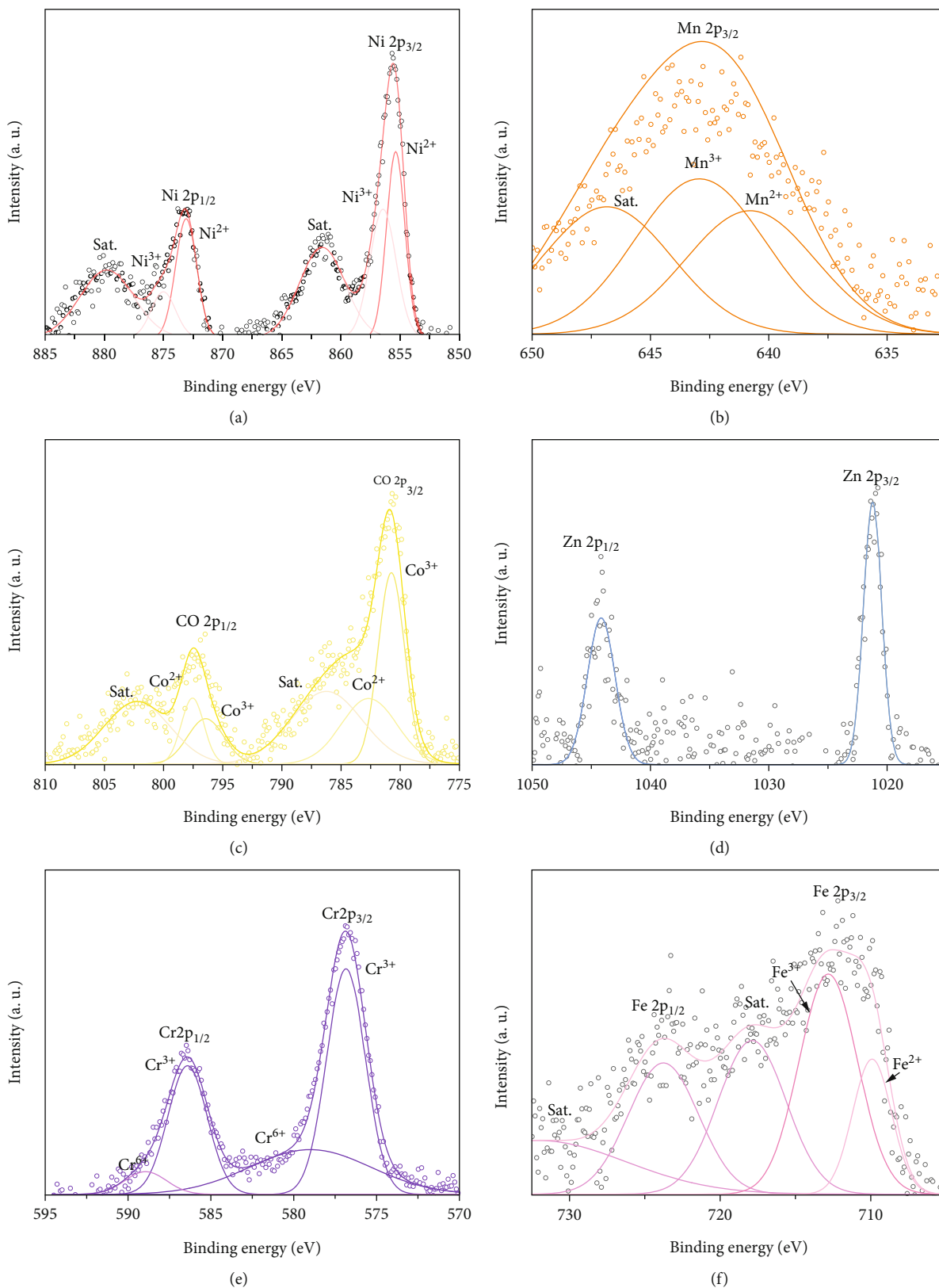
(a)

(b)

(c)

(d)

(e)

(f)

FIGURE 2: XPS spectra of HECs for (a) Ni 2p, (b) Mn 2p, (c) Co 2p, (d) Zn 2p, (e) Cr 2p, and (f) Fe 2p.

clearly revealed the coexistence of all the constituent metallic elements over the surface of the HECs with homogeneous distributions (Figure 1(e)). Furthermore, C and O were uniformly present on the surface, confirming the successful formation of high-entropy carbonates. The XRD patterns of all the samples are shown in Figure 1(f). A single
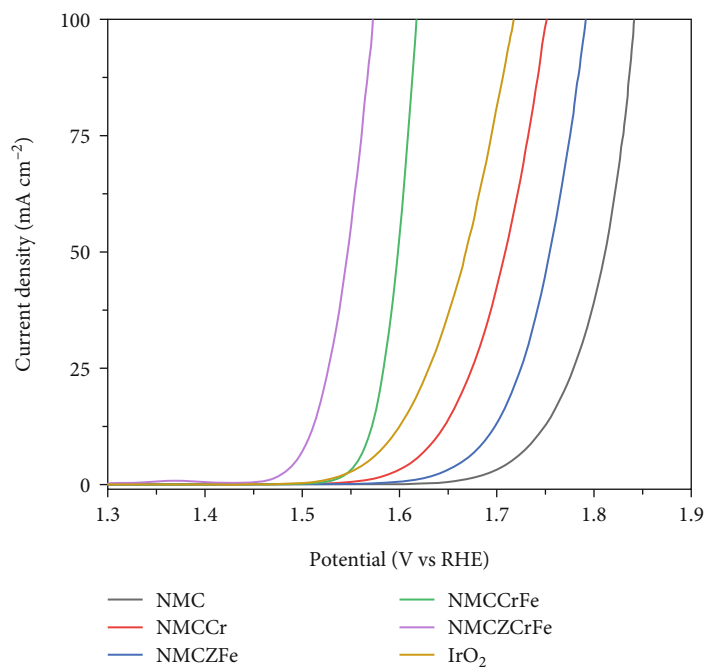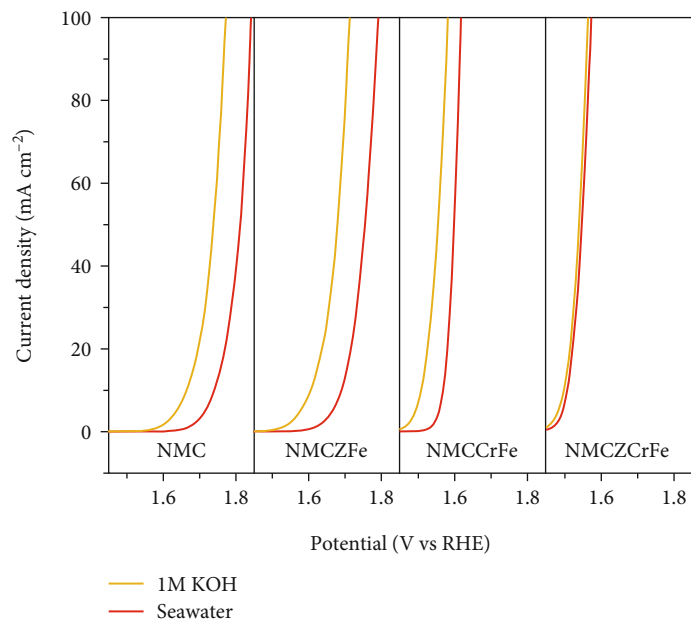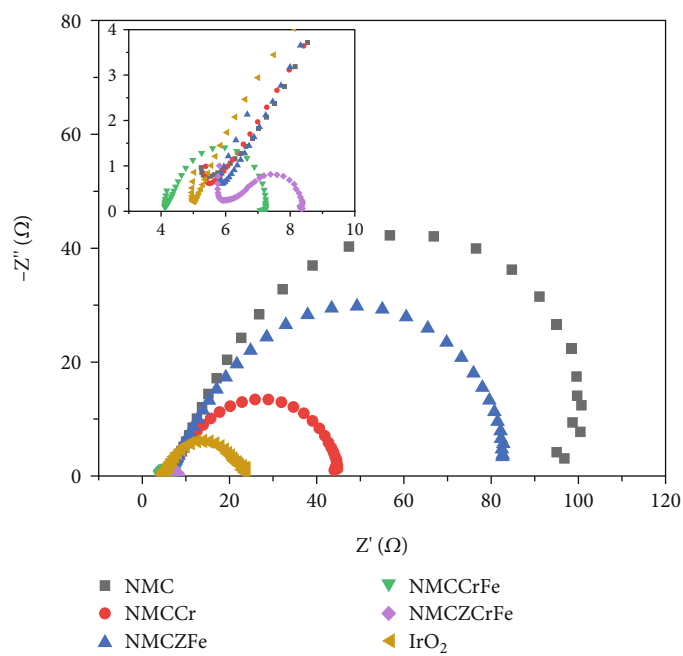
(a)
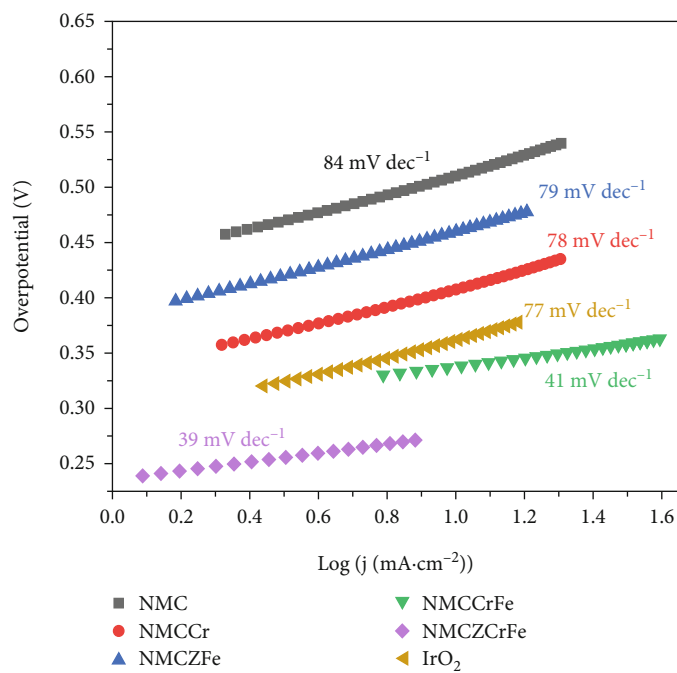
(b)

FIGURE 3: Continued.
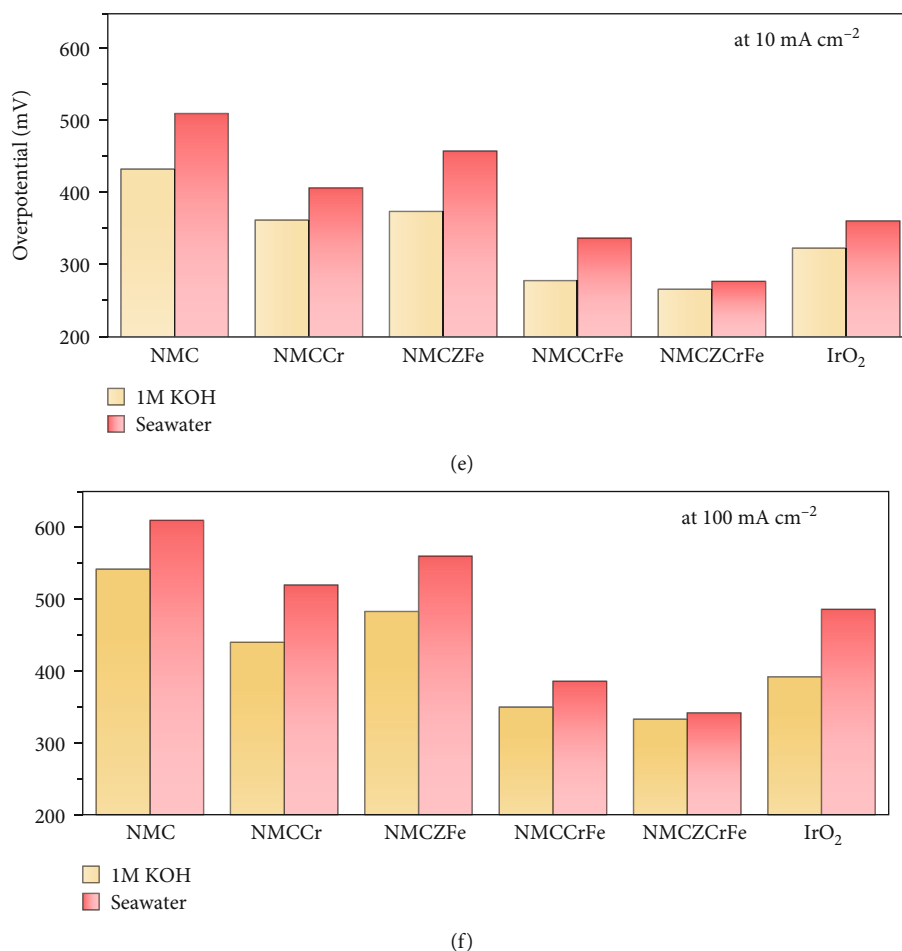
(c)

(d)

Figure 3: Continued.

(e)

(f)

FIGURE 3: (a) LSV polarization curves for OER under alkalized seawater electrolyte and the corresponding (b) Tafel plots for the prepared carbonate samples and the benchmark IrO_2 catalyst. (c) OER activity comparison under alkaline and alkalized seawater electrolytes. (d) Nyquist plots (Z' vs. $-Z''$) of the prepared carbonate samples. (e, f) Summarized overpotentials of the different samples under alkaline and alkalized seawater electrolytes at current densities of 10 and 100 mA cm^{-2}.

carbonate phase was observed in pristine NMC and HEC powders. This indicates the highly entropic nature of the HECs. We have also determined the atomic percentage of each element present in the catalyst using energy dispersive X-ray spectroscopy. In NMCZCrFe, the percentage of Ni, Mn, Co, Zn, Cr, Fe, and O is 3.07, 8.68, 10.01, 0.42, 1.71, 1.28, and 74.83 at%, respectively (Table S1).

The electronic valence states of all the metallic elements in the HECs were analyzed using XPS. Most elements (Ni, Mn, Co, Cr, and Fe) exhibited mixed valence states (Figure 2). Specifically, the 2^+ and 3^+ valence states were detected in the Ni, Mn, Co, and Fe XPS 2p spectra, whereas a mixed valence state of 3^+ and 6^+ was found in the Cr XPS 2p spectra. The detailed peak positions of the respective elements are summarized in Table S2. Notably, the signal for the Zn 2p XPS spectra was too weak to obtain a good fitting result (Figure 2(d)), leading to difficulty in precisely determining the electronic valence state of Zn in the HECs. The high-resolution XPS spectra of the O1s are provided in Figure S2. Both the spectra confirm the presence of CO_3^{2-} in the catalyst. The O1s spectrum shows three peaks labeled as O1, O2, and O3. The peak labelled as O1 is

attributed to the binding of O with metal, the peak labelled as O2 corresponds to the oxygen of the carbonate group (CO_3^{2-}), and the peak labelled as O3 corresponds to the adsorbed H_2O molecules. Similarly, in C1s spectra, three peaks labelled as C1, C2, and C3 correspond to C-O, C=O, and O-C=O linkage of CO_3^{2-}. Given that the electronic flexibility of metallic elements can create more active sites on the catalyst surface with electron-rich or electron-depleted regions, the coexistence of multiple elements with mixed valence states in HECs should benefit the enhancement of the electrocatalytic activity toward the OER. In addition, the dissolution of active metallic elements can be suppressed by efficiently exchanging charges between multivalent metals during electrolysis, leading to improved electrochemical stability. This is studied further in the following discussion.

The electrocatalytic activity for seawater oxidation was evaluated using an alkalized seawater electrolyte, 1 M KOH and 0.5 M NaCl. First, the LSV polarization curves were measured for the prepared samples (Figure 3(a)). The results indicated that the activity trends followed the order NMC < NMCCr < NMCZFe < NMCCrFe < IrO_2 < NMCCrFe < NMCZCrFe (HECs). We have also checked the activity of
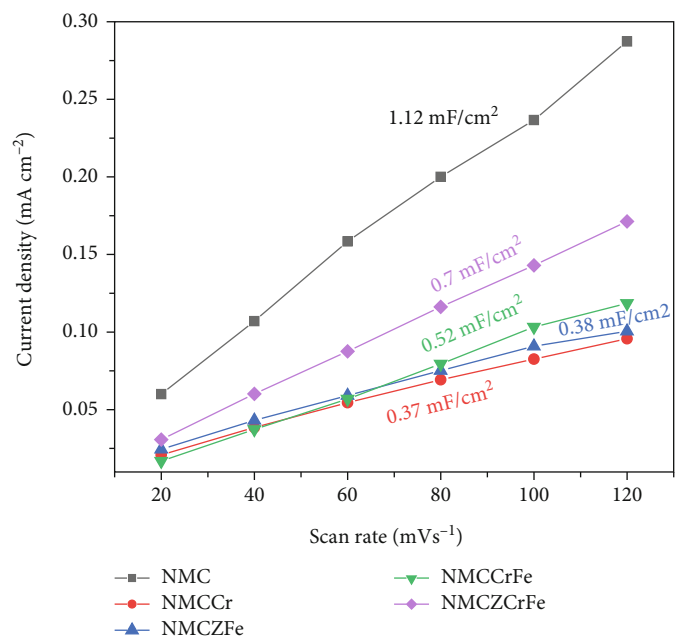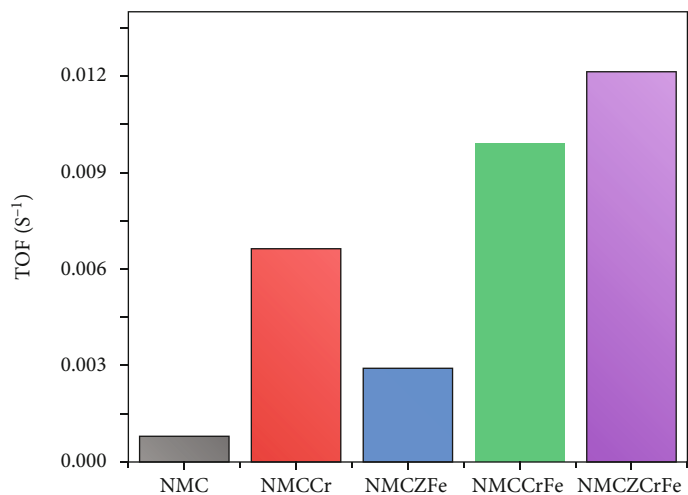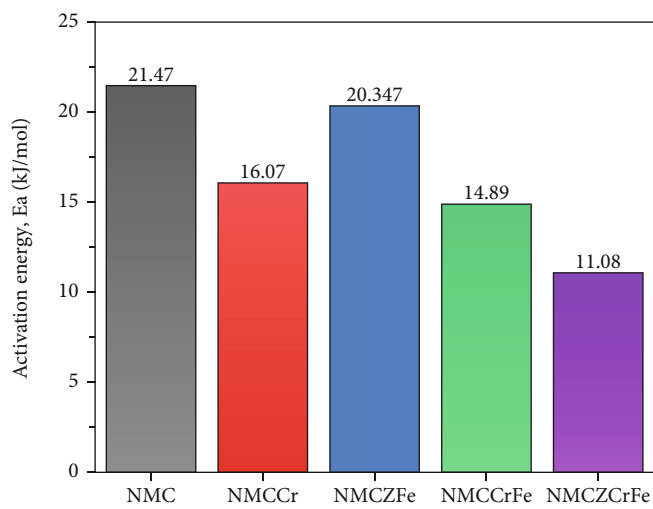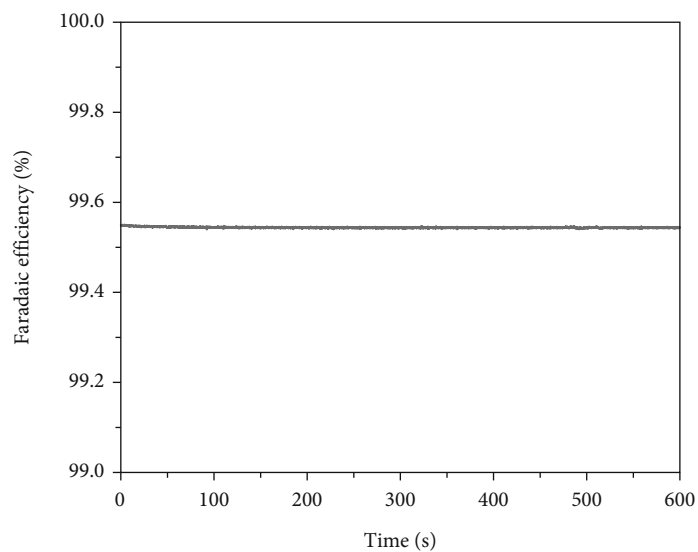
(a)
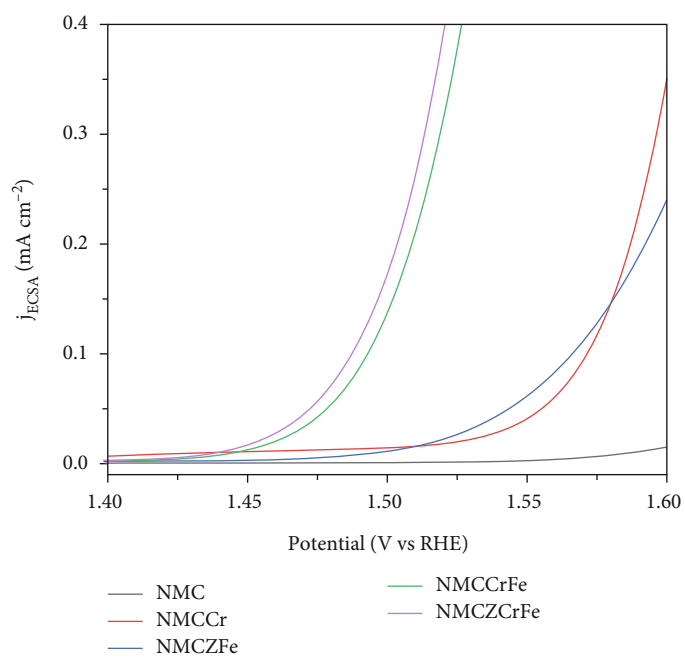
(b)

Figure 4: Continued.

(c)
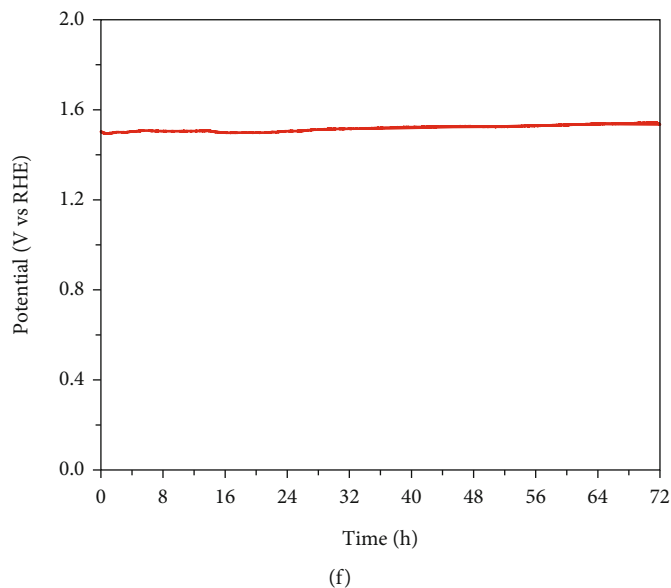

(d)

(e)

FIGURE 4: Continued.

(f)

FIGURE 4: (a) C_{dl} and (b) ECSA normalized LSV curves of the prepared samples. (c) Calculated TOF values and (d) activation energies of the prepared samples. (e) Faradaic efficiency of HECs for seawater oxidation measured by RRDE technique. (f) Stability test of HECs for seawater oxidation using chronopotentiometry measurement.

the other control sample NMCCrZ, NMCFe, NMCCr, and NMCZ, and the polarization curve of these catalysts is provided in Figure S3. The performance of these catalyst is also inferior when compared to the NMCZCrFe. The high catalytic activity for the HECs containing six metal may be due to the synergistic effect arising from the nonuniform distribution of all the atoms of the catalytic surface. We also checked the oxidation and reduction peak of the catalyst using cyclic voltammetry curve (Figure S4); however, the activity obtained from the CV curve is in line with the LSV curves. The Tafel slopes obtained from the LSV curves indicate that the OER kinetics followed the same trend as the catalytic activity (Figure 3(b)). These results highlight that synergetic interactions among multiple metals in HECs are crucial for enhancing their electrocatalytic activity toward seawater oxidation. Furthermore, we tested the catalytic activity of the different carbonate samples under alkaline conditions (1.0 M KOH) while keeping all other measurement conditions identical. The comparative LSV curves for the OER in different electrolytes are summarized in Figure 3(c). Remarkably, the HECs showed a negligible catalytic activity change for alkaline and seawater oxidation, while for the other samples, a noticeable activity drop was observed for seawater oxidation compared to those for the OER in an alkaline electrolyte. The overpotentials at current densities of $10 \, \text{mA cm}^{-2}$ for alkaline and seawater oxidations are summarized in Figure 3(e). Notably, the HECs exhibited overpotentials of 265 and 275 mV for alkaline and seawater oxidation, respectively, which are approximately 434 and 510 mV lower than those of the ternary NMC carbonate. The overpotentials of HECs were even lower than those of the benchmark IrO_2 catalyst (361 mV at $10 \, \text{mA cm}^{-2}$) regardless of electrolytes. This activity trend for the HECs was still true even at a higher current density such as

$100 \, \text{mA cm}^{-2}$ (Figure 3(f)). Furthermore, among the tested samples, the HECs showed the lowest overpotential increase (10 mV) for seawater oxidation compared with the alkaline OER. Thus, the presence of multiple metals in HECs and their electronic interactions may be the key to achieving high catalytic activity under corrosive seawater conditions. In addition, the charge transfer resistance (R_{ct}) was calculated from the Nyquist plots (Z' vs. $-Z''$) (Figure 3(d)). The HECs exhibited the lowest R_{ct} value ($2.2 \, \Omega$) among the tested samples, indicating improved OER kinetics by alloying different metals in a single carbonate framework. The other control sample exhibited high charge transfer resistance which shows the slow diffusion of the intermediate arising from the slow charge transfer through the electrode-electrolyte interface.

To assess the intrinsic catalytic activity, the ECSAs were obtained by calculating the electrochemical double-layer capacitance (C_{dl}) using the CV scan method (Figure S5). The C_{dl} of NMCZCrFe (HECs), NMCCrFe, NMCZFe, NMCCr, and NMC were calculated as 0.7, 0.52, 0.38, 0.37, and $1.12 \, \text{mF cm}^{-2}$, respectively, where the ECSA has a linear relationship with C_{dl} (see Materials and Methods for details) (Figure 4(a)). We obtained the ECSA values of 2.7, 2.0, 1.4, 1.39, and $4.32 \, \text{cm}^2$ for NMCZCrFe (HECs), NMCCrFe, NMCZFe, NMCCr, and NMC, respectively. The higher double-layer capacitance for the precursor NMC is attributed to the more rough surface compared to the other catalysts. When the metal atoms started agglomerated onto the surface of the NMC, the capacity to hold charges decreases resulting in the reduced C_{dl} value. The LSV polarization curves were normalized to the ECSA to represent the intrinsic catalytic activity. Figure 4(b) reveals that the HECs can generate the highest specific current density (j_{ECSA}) at a constant voltage among the tested samples. It was found that the HECs have a lower ECSA compared to that of NMC;
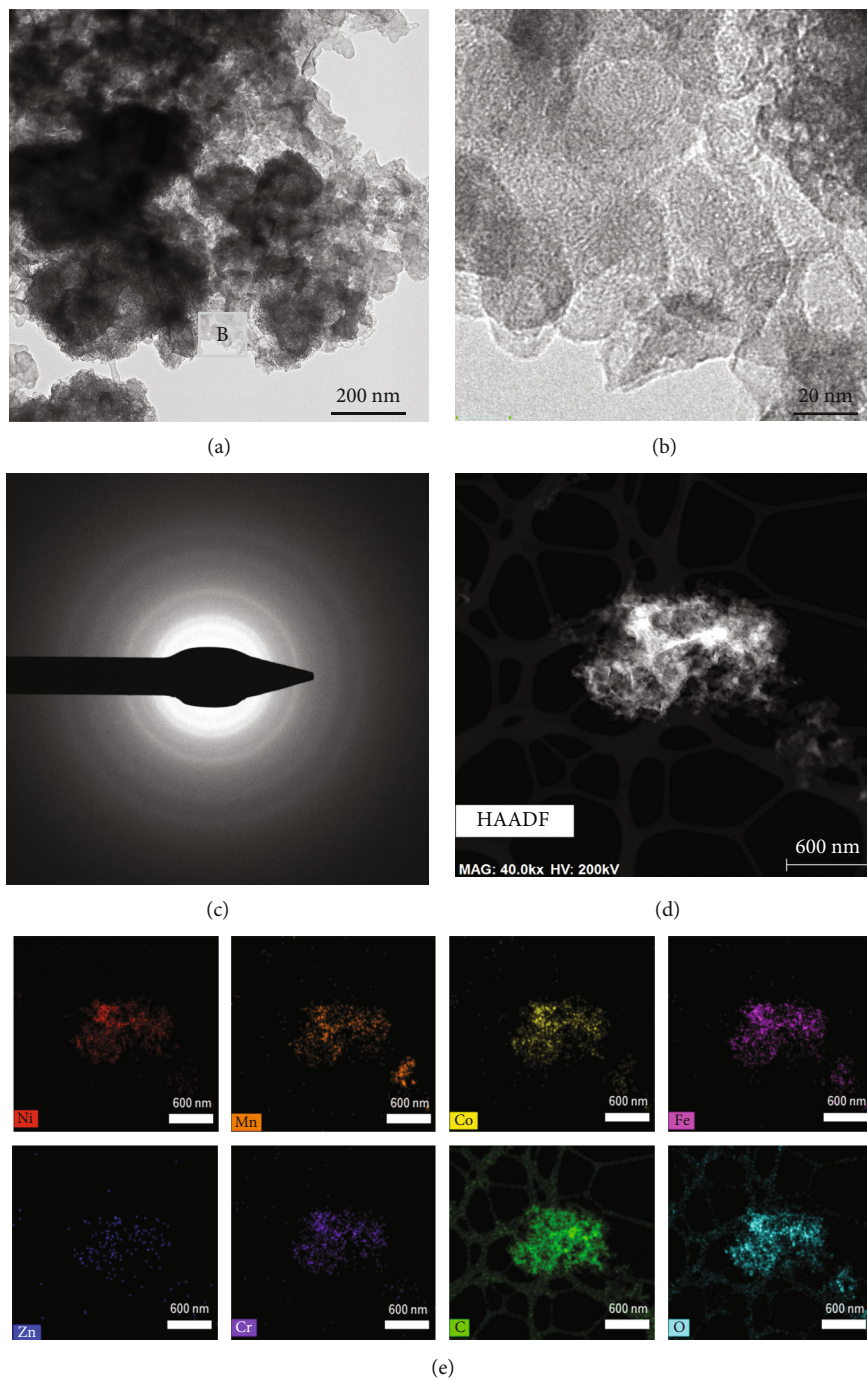
(a)

(b)

(c)
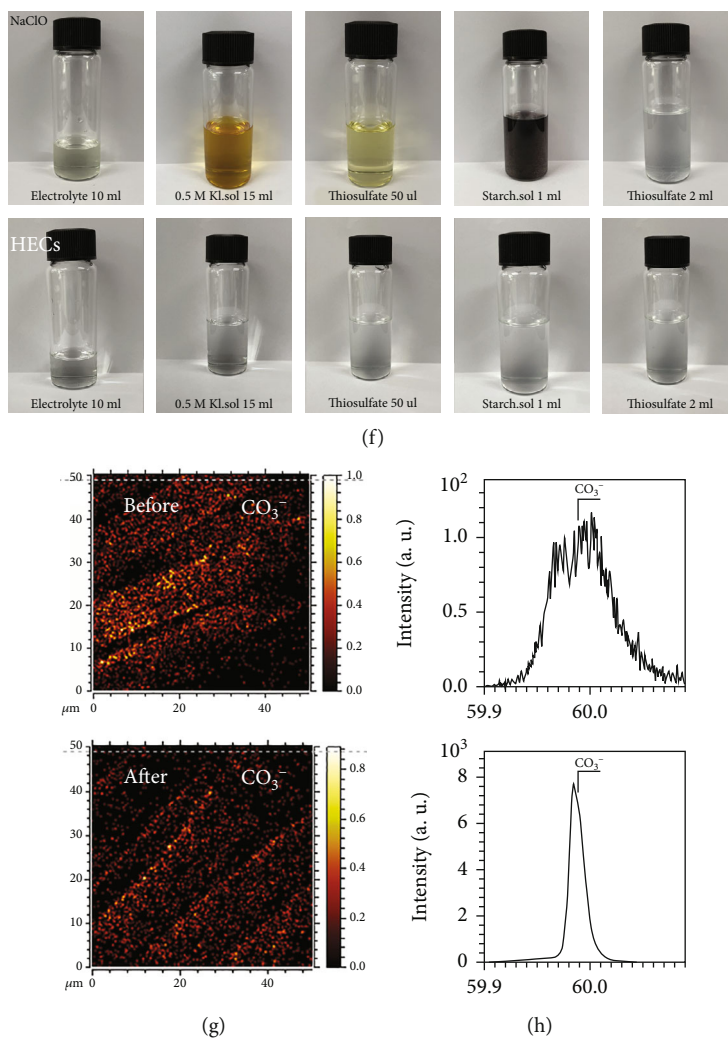

(d)

(e)

Figure 5: Continued.

(f)

(g)

(h)

FIGURE 5: (a, b) TEM images and (c) the SAED pattern of HECs after long-term seawater oxidations. (d) STEM and (e) STEM-EDX mapping results for the post-OER HEC sample. (f) Digital images for iodide titration experiments performed for (lower) the electrolyte after long-term seawater oxidation using the HECs as a catalyst and (upper) the reference (NaClO) solutions, respectively. (g, h) TOF-SIMS results for the HECs before and after seawater oxidations.

however, their j_{ECSA} was much higher than that of the latter (for example, 0.175 and 0.003 mA cm^{-2} at 1.5 V$_{RHE}$). Furthermore, the TOFs and E_a for the OER were calculated, where the HECs showed the most promising values compared to the control samples (Figures 4(c) and 4(d) and Figures S6-S9). These results indicate the enhanced intrinsic catalytic activity of the HECs for seawater oxidation. Given that competitive oxidation reactions, that is, the OER and CER, can occur simultaneously during seawater electrolysis, the selectivity of catalysts, in addition to their intrinsic activity, is crucial for seawater oxidation. Hence, we calculated the FE of the HECs using the RRDE technique, following our previous report [22]. The HECs yielded approximately 99.5% FE for the OER, demonstrating their high catalytic selectivity for the OER against the CER (Figure 4(e)). Finally, a long-term stability of HECs for seawater oxidation was evaluated by using chronopotentiometry at 10 mA cm^{-2} (Figure 4(f)). Notably, a negligible potential increase was observed after continuous seawater electrolysis for 72 h, indicating the good

electrocatalytic stability of the HECs. Electrocatalytic performance of HECs for alkaline seawater oxidations was superior or comparable than the recently reported state-of-the-art catalyst (Table S3). We have also checked the stability of the catalyst at high current density of 100 mA cm^{-2} using chronopotentiometry. The catalyst was able to maintain the potential required to achieve 100 mA cm^{-2} current density for 12 h (Figure S10).

The structural and chemical modulations after seawater electrolysis were studied using ex situ TEM and STEM-EDX analyses. HECs were collected from the electrode surface after 72 h of continuous seawater oxidation for TEM analysis. Although it was difficult to track the precise morphological change during electrolysis owing to the presence of an organic binder, the HECs exhibited a polycrystalline nature after long-term seawater oxidation (Figures 5(a)–5(c)). More importantly, the STEM-EDX mapping results confirmed the coexistence of all the elements present in the pristine HEC sample (Figures 5(d) and 5(e)). The SEM

image after stability is provided in Figure S11, which also shows that there not much change in the morphology of the catalyst after long term-durability test. A quantitative chemical elemental analysis using ICP-OES revealed a relative atomic percentage of 15.15.86 at% (Ni), 21.95 at% (Mn), 21.34 at% (Co), 14.91 at% (Zn), 17.83 at% (Cr), and 8.11 at% (Fe), respectively, in the post-OER NMCZCrFe sample. This clearly indicates that the highly entropic nature of pristine HECs is well preserved during long-term seawater electrolysis.

Furthermore, the high selectivity of the HECs for seawater oxidation against the CER was confirmed through an iodide titration experiment (Figure 5(f)). For the electrolyte collected after seawater oxidation, no color changes were observed during titration, indicating the absence of oxidized chloride species. This implies a high selectivity of the HECs for the OER. The high selectivity could be related to the polyanionic nature of the carbonates in the HECs, which repel negatively charged chloride ions from the catalyst surface. To confirm this hypothesis, we performed an ex situ TOF-SIMS analysis of HECs before and after seawater oxidation. The resulting images and obtained signal profiles for CO_3^{2-} are presented in Figures 5(g) and 5(h), respectively. Notably, CO_3^{2-} was homogeneously present on the surface of the HECs (Figure 5(g)), and the signal for CO_3^{2-} was significantly enhanced after seawater electrolysis (Figure 5(h)). These results indicate that the CO_3^{2-} polyanions in HECs are physiochemically stable during electrochemical reactions and, thus, are advantageous for improving the catalytic selectivity for seawater oxidation by repelling chloride ions. Hence, the direct use of carbonates with highly entropic atomic structures is a promising strategy for developing new catalytic materials for seawater oxidation.

4. Conclusion

The newly developed HECs demonstrate promising catalytic activity and stability for seawater oxidation, opening a new catalyst design strategy for seawater splitting. Synergetic effects among the different elements in HECs were mainly responsible for enhancing the catalytic performance. In addition, the presence of polyanionic CO_3^{2-} in HECs significantly improved the catalytic reaction selectivity toward the OER over the CER in alkalized seawater electrolytes. As a result, the HECs demonstrated a lower overpotential and Tafel slope than control samples, such as ternary NMC, quaternary NMCCr, quinary NMCCrFe/NMCZFe, and a benchmark IrO$_2$ catalyst. The HECs showed negligible degradation of OER activity under different electrolytes and alkaline and alkalized seawater conditions, demonstrating their promising catalytic performance for seawater oxidation. Furthermore, superior intrinsic catalytic activity was confirmed for the HECs. Thus, the use of carbonates with highly entropic atomic configurations is promising for designing next-generation electrocatalysts for seawater oxidation.

Data Availability

Data are available on request from the corresponding authors.

Conflicts of Interest

The authors declare that they have no conflict of interest.

Authors' Contributions

Min Gi Kim and Ashish Gaur contributed equally to this work.

Acknowledgments

Supplementary Materials

The supplementary file contains SEM mapping of NMC, O1s XPS spectra of NMCZCrFe, LSV curves of controlled samples, CV curve in the OER potential range, CV curve for calculating C_{dl}, LSV curves measured at different temperatures, and chronoamperometry curve at 100 mA cm^{-2}, after stability SEM analysis. (Supplementary Materials)

References

[1] T. Rimza, S. Saha, C. Dhand et al., "Carbon-Based Sorbents for Hydrogen Storage: Challenges and Sustainability at Operating Conditions for Renewable Energy," *ChemSusChem*, vol. 15, no. 11, article e202200281, 2022.

[2] L. Vidas and R. Castro, "Recent developments on hydrogen production technologies: state-of-the-art review with a focus on green-electrolysis," *Applied Sciences*, vol. 11, no. 23, article 11363, 2021.

[3] Y. Li, X. Wei, L. Chen, and J. Shi, "Electrocatalytic hydrogen production trilogy," *Angewandte Chemie International Edition*, vol. 60, no. 36, pp. 19550–19571, 2021.

[4] X. Li, X. Hao, A. Abudula, and G. Guan, "Nanostructured catalysts for electrochemical water splitting: current state and prospects," *Journal of Materials Chemistry A*, vol. 4, no. 31, pp. 11973–12000, 2016.

[5] J. Zhang, Z. Zhao, Z. Xia, and L. Dai, "A metal-free bifunctional electrocatalyst for oxygen reduction and oxygen evolution reactions," *Nature Nanotechnology*, vol. 10, no. 5, pp. 444–452, 2015.

[6] C. Singh, S. Mukhopadhyay, and I. Hod, "Metal-organic framework derived nanomaterials for electrocatalysis: recent developments for CO$_2$ and N$_2$ reduction," *Nano Convergence*, vol. 8, no. 1, p. 1, 2021.

[7] G. Fan, F. Li, D. G. Evans, and X. Duan, "Catalytic applications of layered double hydroxides: recent advances and perspectives," *Chemical Society Reviews*, vol. 43, no. 20, pp. 7040–7066, 2014.

[8] H. Zhang, Y. Luo, P. K. Chu et al., "Recent advances in non-noble metal-based bifunctional electrocatalysts for overall

seawater splitting," *Journal of Alloys and Compounds*, vol. 922, article 166113, 2022.

[9] Z. K. Ghouri, K. Elsaid, M. M. Mahmoud Nasef, A. Badreldin, Y. Wubulikasimu, and A. Abdel-Wahab, "Incorporation of manganese carbonyl sulfide ((Mn2S2 (CO)7)) and mixed metal oxides-decorated reduced graphene oxide (MnFeCoO4/rGO) as a selective anode toward efficient OER from seawater splitting under neutral pH conditions," *Renewable Energy*, vol. 190, pp. 1029–1040, 2022.

[10] J. Sun, Z. Zhao, J. Li, Z. Li, and X. Meng, "Recent advances in transition metal selenides-based electrocatalysts: rational design and applications in water splitting," *Journal of Alloys and Compounds*, vol. 918, article 165719, 2022.

[11] Y. Zhang, C. Fu, J. Fan, H. Lv, and W. Hao, "Preparation of Ti@NiB electrode via electroless plating toward high-efficient alkaline simulated seawater splitting," *Journal of Electroanalytical Chemistry*, vol. 901, article 115761, 2021.

[12] L. Yu, Q. Zhu, S. Song et al., "Non-noble metal-nitride based electrocatalysts for high-performance alkaline seawater electrolysis," *Nature Communications*, vol. 10, no. 1, p. 5106, 2019.

[13] S. Dresp, F. Dionigi, M. Klingenhof, and P. Strasser, "Direct electrolytic splitting of seawater: opportunities and challenges," *ACS Energy Letters*, vol. 4, no. 4, pp. 933–942, 2019.

[14] F. Dionigi, T. Reier, Z. Pawolek, M. Gliech, and P. Strasser, "Design criteria, operating conditions, and nickel-iron hydroxide catalyst materials for selective seawater electrolysis," *ChemSusChem*, vol. 9, no. 9, pp. 962–972, 2016.

[15] W.-Y. Huo, S.-Q. Wang, W.-H. Zhu et al., "Recent progress on high-entropy materials for electrocatalytic water splitting applications," *Tungsten*, vol. 3, no. 2, pp. 161–180, 2021.

[16] X. Chang, M. Zeng, K. Liu, and L. Fu, "Phase engineering of high-entropy alloys," *Advanced Materials*, vol. 32, no. 14, article 1907226, 2020.

[17] J.-W. Yeh, S.-Y. Chang, Y.-D. Hong, S.-K. Chen, and S.-J. Lin, "Anomalous decrease in X-ray diffraction intensities of Cu–Ni–Al–Co–Cr–Fe–Si alloy systems with multi-principal elements," *Materials Chemistry and Physics*, vol. 103, no. 1, pp. 41–46, 2007.

[18] R. Zhao, Z. Wang, Q. Xu et al., "Self-supported amorphous iridium oxide catalysts for highly efficient and durable oxygen evolution reaction in acidic media," *Electrochimica Acta*, vol. 391, article 138955, 2021.

[19] Y. Gao, Y. Liu, H. Yu, and D. Zou, "High-entropy oxides for catalysis: Status and perspectives," *Applied Catalysis A: General*, vol. 631, article 118478, 2022.

[20] J. Liu, J. Song, H. Xiao et al., "Synthesis and thermal properties of ZnAl layered double hydroxide by urea hydrolysis," *Powder Technology*, vol. 253, pp. 41–45, 2014.

[21] J. M. Valverde, A. Perejon, S. Medina, and L. A. Perez-Maqueda, "Thermal decomposition of dolomite under CO2: insights from TGA and in situ XRD analysis," *Physical Chemistry Chemical Physics*, vol. 17, no. 44, pp. 30162–30176, 2015.

[22] E. Enkhtuvshin, S. Yeo, H. Choi et al., "Surface reconstruction of Ni–Fe layered double hydroxide inducing chloride ion blocking materials for outstanding overall seawater splitting," *Advanced Functional Materials*, vol. 33, no. 22, article 2214069, 2023.